



Article

Calibration of Phased-Array High-Frequency Radar on an Anchored Floating Platform

Bin Wan , Xiongbin Wu ^{*}, Xianchang Yue , Lan Zhang and Li Wang

Electronic Information School, Wuhan University, Wuhan 430072, China; bwan@whu.edu.cn (B.W.); yuexc@whu.edu.cn (X.Y.); zhanglan@whu.edu.cn (L.Z.); warren@whu.edu.cn (L.W.)
^{*} Correspondence: xbwu@whu.edu.cn; Tel.: +86-189-9564-0072

Abstract: Prior studies have highlighted the importance of calibrating receiver antennas in target direction-of-arrival (DOA) estimation and surface current measurement for high-frequency (HF) radar systems. It is worth noting that the calibration contributes to the performance of both shore-based HF radar and platform-mounted HF radar. Compared with shore-based HF radar, the influence of six-degrees-of-freedom (six-DOF) platform motion should be considered in the calibration of platform-mounted HF radar. This paper initially describes a calibration scheme that receives phased-array antennas for an anchored platform-mounted HF radar incorporating a model of free rotation, which is called yaw rotation and dominates the six-DOF platform motion in this study. In the presence of yaw rotation, the amplitude and phase of the source calibration signal from the other shore-based radar sites reveal the directional sensitivity of the receiver phased-array antennas. The calibration of receiver phased-array antennas is composed of channel calibration (linking cables and receiver hardware calibration) and antenna pattern calibration. The antenna pattern at each bearing can be represented by the Fourier series. The estimation of channel calibration and antenna pattern calibration depends on an overdetermined HF radar system consisting of observed values and theoretical constraints, so the least-squares fits of the channel calibration coefficients and antenna pattern calibration coefficients are obtained. The experimental results show that the target DOA estimation and surface current measurement can be improved if the phased-array platform-mounted HF radar system is calibrated.

Keywords: calibration; phased-array; high-frequency (HF) radar; platform-mounted



Citation: Wan, B.; Wu, X.; Yue, X.; Zhang, L.; Wang, L. Calibration of Phased-Array High-Frequency Radar on an Anchored Floating Platform. *Remote Sens.* **2022**, *14*, 2174. <https://doi.org/10.3390/rs14092174>

Academic Editor: Chang-Wook Lee

Received: 28 March 2022

Accepted: 25 April 2022

Published: 30 April 2022

Publisher's Note: MDPI stays neutral with regard to jurisdictional claims in published maps and institutional affiliations.



Copyright: © 2022 by the authors. Licensee MDPI, Basel, Switzerland. This article is an open access article distributed under the terms and conditions of the Creative Commons Attribution (CC BY) license (<https://creativecommons.org/licenses/by/4.0/>).

1. Introduction

High-frequency (HF) radar systems are currently invaluable instruments for measuring ocean surface currents. Crombie [1] deduced the Bragg scattering mechanism accounting for the two strong peaks appearing above and below the carrier frequency in the Doppler spectrum. The Bragg peaks are echoes diffracted from the ocean waves of one-half the radar wavelength and running towards and away from the radar. The theoretical Bragg frequency in the Doppler spectrum is proportional to the phase velocity of the Bragg ocean waves. The difference between the theoretical Bragg frequency and measured values of Doppler shift could be used to measure the radial component of the surface current velocity relative to the radar site [2]. The total vector surface current is produced by combining at least two radial current measurements into a vector current based on the geometric constraints of the radar site configuration [3]. In recent years, surface currents have been applied for civil purposes. Measured surface current data have been used to detect tsunami arrivals [4–7] and oil spill trajectories [8–11].

There are two types of HF radar-receiving antennas: monopole-crossed-loop antennas and phased-array antennas. The use of a direction-finding algorithm such as Multiple Signal Classification (MUSIC) [12–16] is a common technique employed to estimate the direction-of-arrival (DOA) of sea echo signals. Positioning the radial current at a bearing

within a given range depends on estimating the DOA corresponding to each radial current speed. A crucial factor for estimating DOAs is determining the amplitude and phase errors caused by the antenna pattern distortions and channel distortions (linking cables and receiver hardware distortions). Accordingly, the calibration of receiver phased-array antennas plays a vital role in estimating the DOA and measuring surface currents [17–20].

For shore-based HF radars, several methods have been used in practical HF radar systems to conduct array calibrations. The conventional calibration of a shore-based HF radar system is implemented by means of a transponder or stable radio signal traveling in arcs around individual shore-based radar sites [17]. Subsequently, single-DOA sea echoes are utilized to conduct array calibrations based on the shift-invariance antenna pairs in the phased-array in the HF radar [21]. In recent years, one method for calibrating phased-array antennas was to employ ships of opportunity with unknown ship positions based upon the least-squares method [22–24]. In contrast, the ships of opportunity with known positions depending on the automatic identification system (AIS) transmitters are used to obtain the calibrated antenna patterns and channel calibration coefficients [25–28]. Furthermore, Washburn et al. [29] took advantage of the popular and practical aerial drone technique to obtain the calibrated antenna patterns.

Moreover, array calibration, including antenna pattern calibration and channel calibration, is beneficial to the performance of both shore-based HF radars and platform-mounted HF radars. An HF radar operating on an offshore platform [30–34] can meet the remote sensing requirements for obtaining ocean information farther away from the coast. However, when floating on the surface, the platform is subjected to six-degrees-of-freedom (six-DOF) motion (sway translation, surge translation, heave translation, roll rotation, pitch rotation, and yaw rotation) due to interactions with the ocean. Compared with shore-based HF radars, the influence of six-DOF platform motion should be taken into consideration in the array calibration for platform-mounted HF radars. In addition, the calibration signal cannot be extracted directly in the Doppler spectrum, since the Doppler spectrum has been modulated by the platform motion. There are few published reports that attempt to calibrate an anchored platform-mounted HF radar. In this paper, we put forward a calibration scheme to implement reliable DOA estimations and ocean surface current measurements for an anchored platform-mounted HF radar.

This paper documents a calibration scheme of receiver phased-array antennas for an anchored platform-mounted HF radar when the transmitting antenna and receiver antennas are mounted on a platform incorporating a model of free yaw rotation. Between the end of 2016 and the beginning of 2017, an HF radar mounted on a platform anchored on the ocean surface, as part of a distributed HF radar network, was deployed to measure ocean surface currents far from a coastal area. In this study, the yaw rotation is the predominant motion in the six-DOF platform motion and can cover a broad range. In recent years, Yao et al. [35,36,37] revealed the additional peaks caused by oscillations of yaw rotation. In this study, the calibration of the phased array is combined with the yaw rotation. From an analysis of the source calibration signal from the other shore-based HF radar site, the amplitude and phase of the source calibration signal are directional in the presence of yaw rotation. The calibration, including channel calibration coefficients and antenna patterns, is based on an overdetermined HF radar system involving observed values and theoretical constraints, so the least-squares fits of channel calibration coefficients and antenna patterns are obtained. Subsequently, the experimental results show that the DOA estimation and ocean surface current measurement can be improved if the channel calibration coefficients and calibrated antenna patterns are used.

In this paper, Section 2 describes the deployment of an HF radar network involving platform-mounted HF radars and how the channel calibration coefficients and antenna patterns are estimated. The verification results are shown in Section 3. Section 4 presents the discussion. Section 5 contains the conclusions.

2. Materials and Methods

2.1. Introduction of the HF Radar Network

In the last three decades, the importance of an integrated HF radar network has been widely recognized and utilized [38–43]. For an HF radar network, several HF radar sites can operate independently and synchronously based on the Global Positioning System (GPS). Data were obtained from a distributed HF radar network in the Taiwan Strait between the end of 2016 and the beginning of 2017, which consists of three radar sites: one platform-mounted site (a ship, $23^{\circ}42'9''\text{N}$, $117^{\circ}51'37''\text{E}$) and two shore-based sites called Chihu (ChHU, $24^{\circ}2'13''\text{N}$, $117^{\circ}54'9''\text{E}$) and Dongshan (DoSA, $23^{\circ}39'25''\text{N}$, $117^{\circ}29'2''\text{E}$). Figure 1 shows the study area of the distributed HF radar network, and Figure 2 displays the platform (ship) and the circular phased-array consisting of eight receiver antennas.

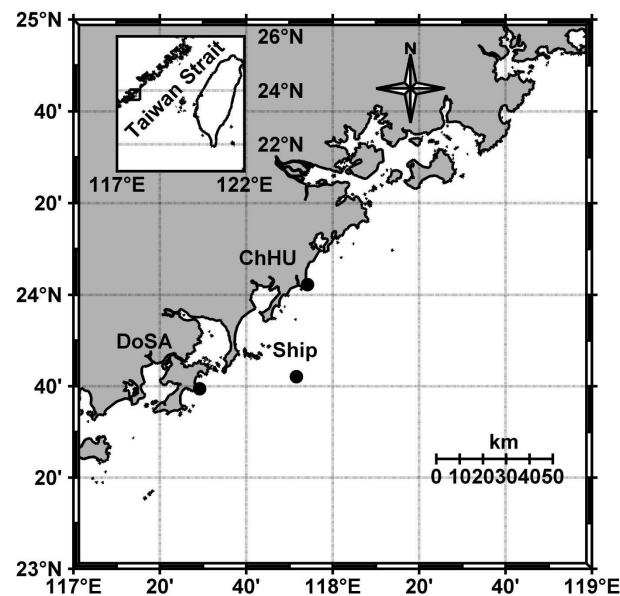


Figure 1. Location of the distributed HF radar network including three radar sites (black dots): the ChHU site, the DoSA site, and the ship site.



Figure 2. Anchored ship platform and circular phased-array receiver antennas consisting of eight monopole elements.

The parameters of an HF radar, the ocean state monitoring and analyzing radar (OSMAR), which was developed by Wuhan University, are introduced in Table 1. The operating frequency is $f_0 = 13.15$ MHz, and $\lambda = 22.8$ m is the wavelength of the transmitted signal. If a linear-current-profile model [44] is assumed, the effective measurement depth

is $\frac{\lambda}{8\pi} = 0.9$ m. Under a logarithmic-current-profile model assumption [45], the effective measurement depth is $\frac{\lambda}{14\pi} = 0.5$ m. The effective depth is considered to be between $\frac{\lambda}{14\pi}$ and $\frac{\lambda}{8\pi}$ (0.5~0.9 m) [46,47]. Every radar site makes use of a frequency-modulated interrupt continuous wave (FMICW) waveform. The sweep period of FMICW is 0.5 s. The range resolution of HF radar is $\Delta R = 5$ km. In addition, the Doppler coherent integration time (CIT) is 5 min or 10 min.

The flowchart of this method, called “yaw-rotation calibration” (YRC) and used in the DOA estimation and ocean surface measurement, is shown in Figure 3 and includes six main steps: platform motion analysis, extraction of the calibration signal for each yaw angle, calculation of the array calibration coefficients, motion compensation and MUSIC algorithm, DOA estimation, and surface current radial velocity measurement.

Table 1. Ocean state monitoring and analyzing radar (OSMAR) parameters

Radar Site	Site 1	Site 2	Site 3
Site Code	Ship	DoSA	ChHU
Latitude	23°42'9"N	23°39'25"N	24°2'13"N
Longitude	117°51'37"E	117°29'2"E	117°54'9"E
Operation Frequency		13.15 MHz	
Transmitted Wave Length		22.8 m	
Measurement Depth		0.5~0.9 m @ 13.15 MHz	
Waveform		FMICW	
Sweep Period		0.5 s	
Range Resolution		5 km	
Number of Transmitter Antenna Elements		1	
Number of Receiver Antenna Elements (Phased-Array)		8	
Technique for Azimuthal Resolution		Direction-finding	
Doppler Coherent Integration Time (CIT)		5 min or 10 min	

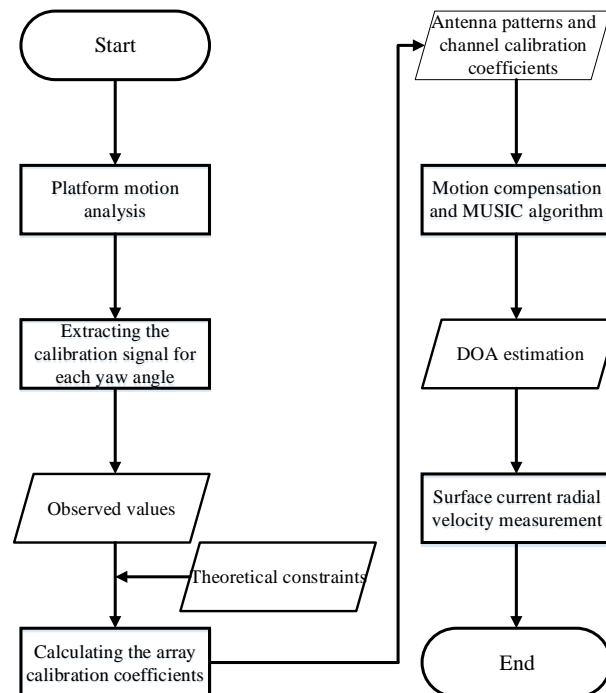


Figure 3. Flowchart of the proposed method (YRC) used in the DOA estimation and surface current radial velocity measurement, including six main steps: platform motion analysis, extraction of the calibration signal for each yaw angle, calculation of the array calibration coefficients, motion compensation and MUSIC algorithm, DOA estimation, and surface current radial velocity measurement.

2.2. Platform Motion Analysis

Platform motion results in time variation for the steering vector of the receiver phased-array antenna [48]. In addition, platform motion causes a broadening of the first-order echo to be superimposed on the continuum, and the platform displacement spectra measured by accelerometers mounted on a platform can be input into an algorithm to remove this effect in the inversion of the ocean surface parameters [30]. Hence, the installation of an accelerometer that records the platform motion data is necessary. An accelerometer consisting of two GPS antennas, the main controller, linking cables, and power supply was installed along the bow direction of the ship to record information about the ship motion attitude every 0.1 s starting at 1300 UTC+8 25 December 2016 and ending at 1300 UTC+8 26 December 2016, where UTC+8 means Universal Time Coordinated 8th Time Zone (East). Real-time attitude data were obtained by an accelerometer, including the easterly speed, northerly speed, upward speed, roll angle, pitch angle, and heading information. Emphatically, the heading information is defined as the clockwise angular discrepancy between due north and the bow direction (y axis) of the ship, which is called the yaw angle α_y herein (see Figure 4c) [49].

The influence analysis based on platform motion is discussed in the Appendix A of this paper. According to this analysis, a moving antenna array is mainly affected by the yaw rotation. Accordingly, the receiver phased-array calibration should be combined with the yaw rotation. The yaw angle (limited from -180° to 180°) curves in the first 10 min and 1 day (the yaw angle largely remains stable in a time span of 1 s) are shown in Figure 5a,b. According to the histogram of the yaw angles (Figure 5c), large angular sectors of the array calibration can be obtained on a time scale of one day.

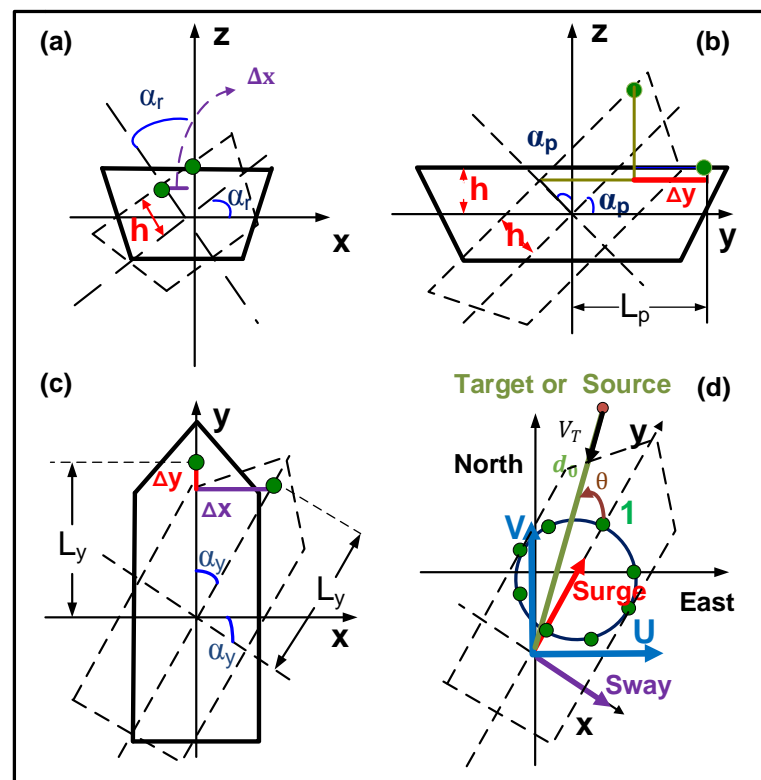


Figure 4. Kinematics of the platform motion (Ant. 1): (a) roll rotation, (b) pitch rotation, (c) yaw rotation, (d) easterly and northerly movement.

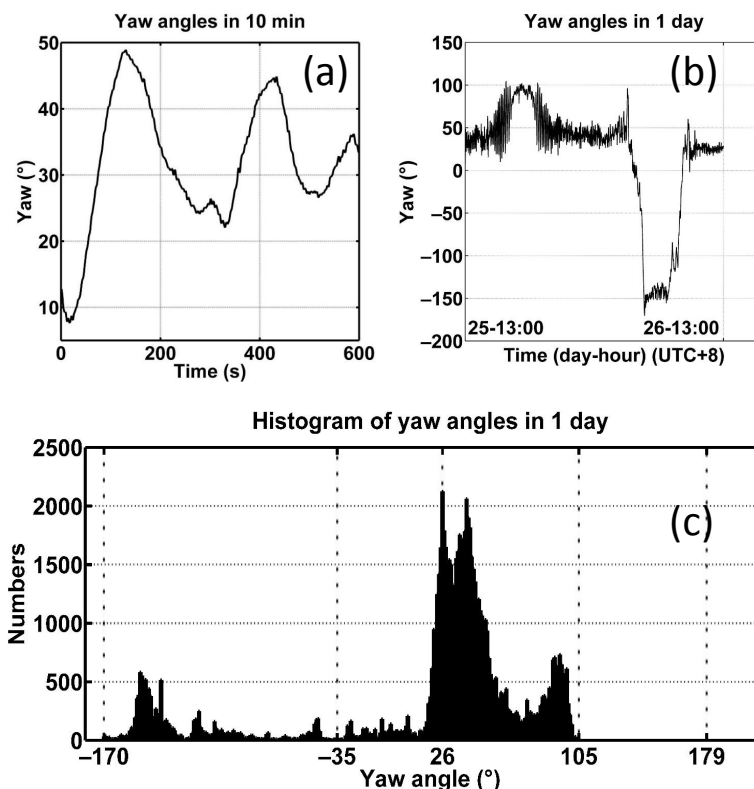


Figure 5. Yaw angles: (a) first 10 min (time span 1 s); (b) 1 day (time span 1 s); (c) histogram of yaw angles in 1 day.

2.3. Extracting the Source Calibration Signal for Each Yaw Angle

In this distributed HF radar network, every radar site can receive echoes from the local (monostatic measurement) and other radar sites (bistatic measurement). Figure 6a shows a geometric sketch of the bistatic HF radar configuration, where Rx and Tx represent the ship site and ChHU radar sites, respectively. The radio signal straight from the ChHU site (the direction of the baseline) can be used as the source calibration signal. Figure 7a shows the range-Doppler spectra received by the ship radar site, where the central, top, and bottom signals represent echoes from the ocean surface caused by the signals transmitted from the local radar site, the ChHU radar site, and the DoSA radar site, respectively. The radio signals straight from the ChHU and DoSA sites are labeled by the red and black ellipses in the range-Doppler spectra, respectively.

In this study, radio signals straight from the ChHU site can be extracted in the range cell number of 40 from the range domain (red ellipse, Figure 7b) every 0.5 s (a sweep period) rather than the Doppler domain. There are two amplitude or phase values in 1 s (a time span) at each yaw angle, and the median value is the required value. Note that $L = 38$ km is the distance from the ChHU site to the ship site. The total range cell number of 40 consists of the real bistatic range cells, $\frac{L}{2 \times \Delta R} = \frac{38}{2 \times 5} \approx 4$ ($2 \times \Delta R = 10$ km is the range isoline width of the bistatic radar) and the pseudorange cells, 36, derived from the artificial time delay in the FMICW waveform design, which is responsible for the shift in the range domain to prevent overlapping.

When the yaw angles range from -170° to 105° , the corresponding ChHU DOA bearing with respect to the y axis is from -177° to 98° . Note that the DOA bearing θ , limited to the range from -180° to 180° , is defined as the angle counterclockwise from the y axis (as the normal to the receiver array) to the baseline direction (see Figure 4d or Figure 6b). The conversion relation is described as $\theta = \alpha_y - \alpha_{BL}$, where α_y is the measured yaw angle and α_{BL} is the angle clockwise from true north to the baseline direction.

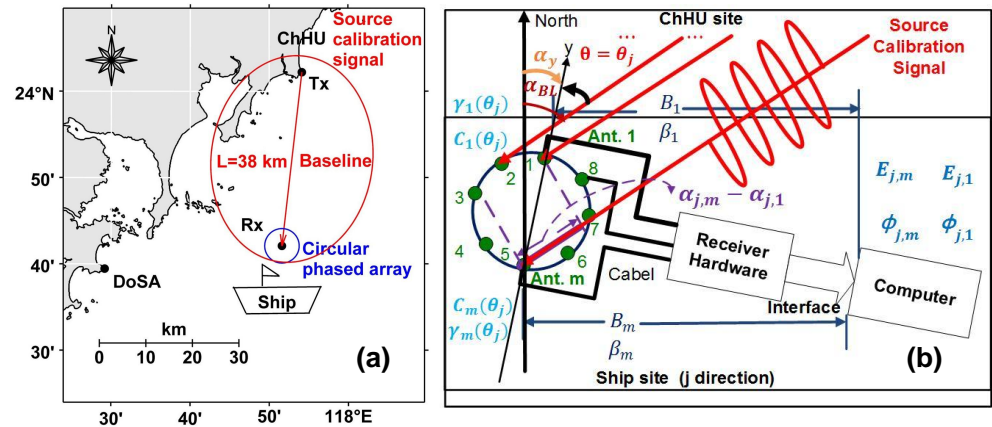


Figure 6. Bistatic geometry of the ChHU and ship sites: (a) sketch of the bistatic geometry (Tx: ChHU radar site, Rx: ship radar site); (b) detailed drawing of the source calibration signal path (from the receiver antennas to the computer). The phase relative to Ant. 1 $\phi_{j,m} - \phi_{j,1}$ at bearing $\theta = \theta_j$ is extracted from the range spectra, which result from the antenna patterns $\gamma_m(\theta_j) - \gamma_1(\theta_j)$, wave path difference $\alpha_{j,m} - \alpha_{j,1}$, and linking cables and receiver hardware $\beta_m - \beta_1$; the amplitude relative to Ant. 1 is $E_{j,m}/E_{j,1}$ at bearing $\theta = \theta_j$, which results from the antenna patterns $C_m(\theta_j)/C_1(\theta_j)$, and linking cables and receiver hardware B_m/B_1 .

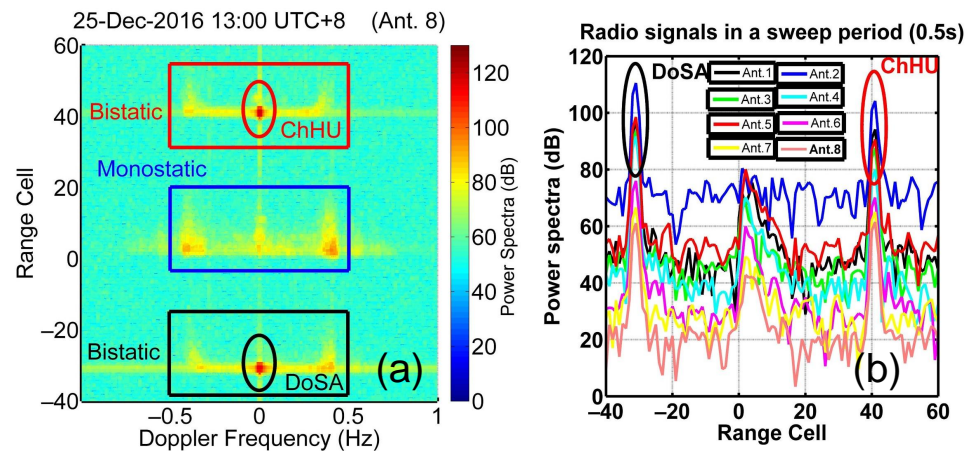


Figure 7. (a) Range-Doppler spectra at 1300 UTC+8 25 December 2016 including one monostatic (blue rectangle) and two bistatic measurements (red and black rectangles) received by the ship radar site (Ant. 8); (b) range spectra in a sweep period (0.5 s) including radio signals from the ChHU site (red ellipse) and the DoSA site (black ellipse).

2.4. Calculating the Array Calibration Coefficients (Channel Calibration Coefficients and Calibrated Antenna Patterns)

The radio signal phases of the antenna number m ($m = 1, 2, \dots, 8$) (hereafter abbreviated as Ant. m) received at every DOA bearing $\theta_j = j - 178$ ($j = 1, 2, \dots, 276$) are $\phi_{j,m}$ (unit: $^\circ$), and the radio signal amplitudes are $E_{j,m}$ (Unit: V) or $E_{dBj,m} = 20 \cdot \log_{10}(E_{j,m})$ (unit: dBm) (Figure 6b).

Figure 5c shows that the angle with maximal emergence probability at all yaw angles is 26° (or a ChHU DOA bearing of 19°), and the angle with minimal probability is the yaw angle -35° (or a ChHU DOA bearing of -42°). Figure 8a,b show the relative phase with respect to Ant. 1 (the reference antenna) $\phi_{j,m} - \phi_{j,1}$ at yaw angles of 26° and -35° . The median values are the required values. Furthermore, Figure 8c,d show the relative amplitude with respect to Ant. 1 $E_{dBj,m} - E_{dBj,1}$ at yaw angles of 26° and -35° . Note that

some distorted values for $\phi_{j,m} - \phi_{j,1}$ at 26° are removed. As shown in Figure 6b, $E_{j,m} \cdot e^{i\phi_{j,m}}$ relative to $E_{j,1} \cdot e^{i\phi_{j,1}}$ consists of three parts, as described below:

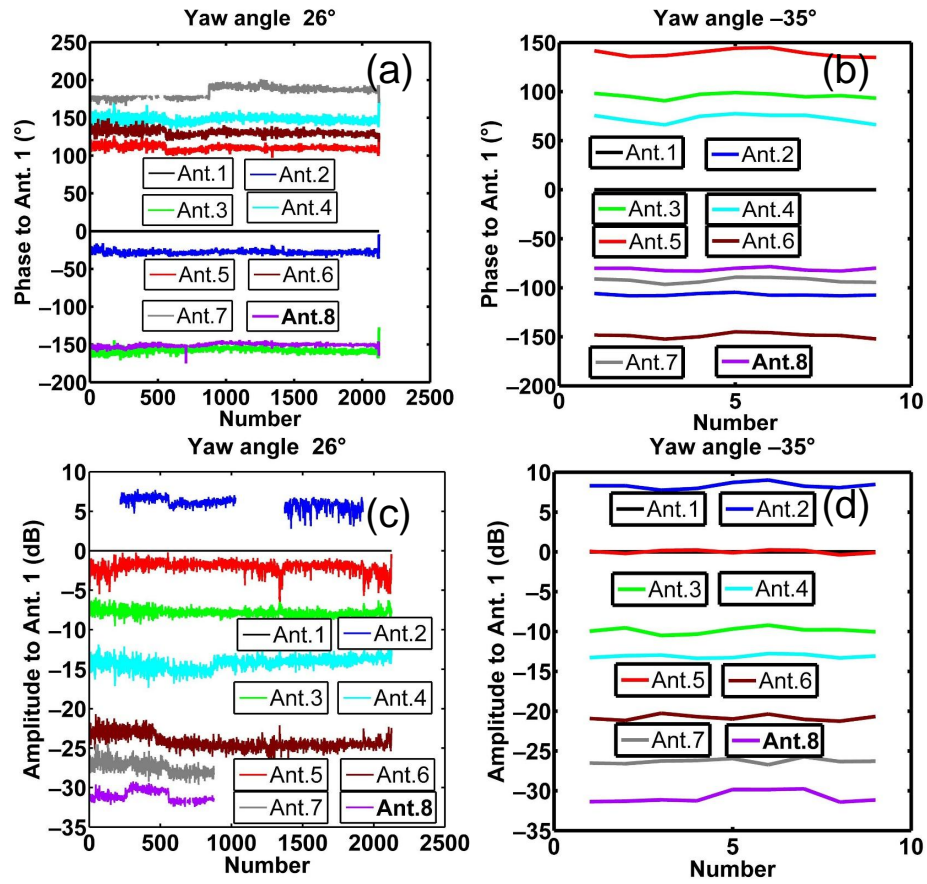


Figure 8. Measured phase relative to Ant. 1: (a) at 26° (DOA bearing of 19°) and (b) at -35° (DOA bearing of -42°); measured amplitude relative to Ant. 1: (c) at 26° (some distorted values are removed) and (d) at -35° .

$$\frac{e^{i\phi_{j,m}}}{e^{i\phi_{j,1}}} = \frac{e^{i\alpha_{j,m}}}{e^{i\alpha_{j,1}}} \cdot \frac{e^{i\beta_m}}{e^{i\beta_1}} \cdot \frac{e^{i\gamma_m(\theta_j)}}{e^{i\gamma_1(\theta_j)}} = e^{i(\alpha_{j,m} - \alpha_{j,1})} \cdot e^{i(\beta_m - \beta_1)} \cdot e^{i[\gamma_m(\theta_j) - \gamma_1(\theta_j)]} \quad (i = \sqrt{-1}) \quad (1)$$

$$\text{or } \phi_{j,m} - \phi_{j,1} = (\alpha_{j,m} - \alpha_{j,1}) + (\beta_m - \beta_1) + [\gamma_m(\theta_j) - \gamma_1(\theta_j)]$$

and

$$\frac{E_{j,m}}{E_{j,1}} = \frac{B_m}{B_1} \cdot \frac{C_m(\theta_j)}{C_1(\theta_j)} \quad (2)$$

$$\text{or } E_{dB_{j,m}} - E_{dB_{j,1}} = (B_{dB_m} - B_{dB_1}) + [C_{dB_m}(\theta_j) - C_{dB_1}(\theta_j)],$$

where $\theta_j = j - 178$ ($j = 1, 2, \dots, 276$), and $m = 1, 2, \dots, 8$. In Equation (1), $\alpha_{j,m} - \alpha_{j,1}$ denotes the constant phase error caused by the wave path difference in every direction among the antennas. In Equations (1) and (2), $\beta_m - \beta_1$ and $B_{dB_m} - B_{dB_1}$ are called the channel calibration coefficients of the phase and amplitude and are the phase and amplitude differences from Ant. m with respect to Ant. 1 caused by the linking cables and receiver hardware between the receiving antennas and the computer, respectively; $\gamma_m(\theta_j) - \gamma_1(\theta_j)$ and $C_{dB_m}(\theta_j) - C_{dB_1}(\theta_j)$ are the phase and amplitude differences caused by the anisotropy of the receiving antenna, respectively.

The phase pattern describes the phase response of the receiving antennas to a given signal as a function of the DOA bearing [25]. Hence, a common and advantageous rep-

representation for every phase response versus the DOA bearing ($-180^\circ \leq \theta < 180^\circ$) is to expand the response into a Fourier series. Accordingly, the estimation of the phase patterns depends on solutions to an unknown Fourier series. The phase patterns are substituted by a Fourier series in the following equation.

$$\gamma_m(\theta) = \sum_{n=0}^N [a_{n,m} \cos(n \times \theta \times \pi/180) + b_{n,m} \sin(n \times \theta \times \pi/180)], \quad (3)$$

where n is the order of the Fourier series, N is the total number of Fourier series, $a_{n,m}$ and $b_{n,m}$ are Fourier coefficients, and $\cos(n \times \theta \times \pi/180)$ and $\sin(n \times \theta \times \pi/180)$ are Fourier basis functions.

Equation (1) is represented as follows:

$$(\beta_m - \beta_1) + \left\{ \sum_{n=0}^N [a_{n,m} \cos(n \times \theta_j \times \pi/180) + b_{n,m} \sin(n \times \theta_j \times \pi/180)] - \sum_{n=0}^N [a_{n,1} \cos(n \times \theta_j \times \pi/180) + b_{n,1} \sin(n \times \theta_j \times \pi/180)] \right\} = (\phi_{j,m} - \phi_{j,1}) - (\alpha_{j,m} - \alpha_{j,1}). \quad (4)$$

We can mark $\beta_{21} = \beta_2 - \beta_1, \dots$, and $\beta_{81} = \beta_8 - \beta_1$, and $\phi_{21} - \alpha_{21} = [(\phi_{1,2} - \phi_{1,1}) - (\alpha_{1,2} - \alpha_{1,1}), (\phi_{2,2} - \phi_{2,1}) - (\alpha_{2,2} - \alpha_{2,1}), \dots, (\phi_{276,2} - \phi_{276,1}) - (\alpha_{276,2} - \alpha_{276,1})]^T, \dots$, and $\phi_{81} - \alpha_{81} = [(\phi_{1,8} - \phi_{1,1}) - (\alpha_{1,8} - \alpha_{1,1}), (\phi_{2,8} - \phi_{2,1}) - (\alpha_{2,8} - \alpha_{2,1}), \dots, (\phi_{276,8} - \phi_{276,1}) - (\alpha_{276,8} - \alpha_{276,1})]^T$ (the superscript "T" indicates transposition).

Note that the uncalibrated patterns of the "monopole" antennas used in this experiment are theoretically perfect; they are assumed to be 1 ($e^{i\gamma_m} = 1$ or $\gamma_m = 0$) in the horizontal plane. Hence, we can add the constrained equations such that the phase patterns at each $N_{Interval}$ degree interval ensure that the actual patterns become perfect as much as possible. The constraint equation is expressed as follows:

$$\gamma_m(\theta_\ell) = \sum_{n=0}^N [a_{n,m} \cos(n \times \theta_\ell \times \pi/180) + b_{n,m} \sin(n \times \theta_\ell \times \pi/180)] = 0, \quad (5)$$

where $\theta_\ell = -180 + (\ell - 1) \times N_{Interval}$ ($\ell = 1, 2, \dots, \lfloor 360/N_{Interval} \rfloor$), and $\lfloor 360/N_{Interval} \rfloor$ is the maximum integer value less than or equal to $360/N_{Interval}$.

It is assumed that the performance of eight antennas is identical according to the symmetric relation with respect to the y axis between Ant. 2 and Ant. 8, between Ant. 3 and Ant. 7, and between Ant. 4 and Ant. 6. In addition, the self-symmetric relation of Ant. 1 also exists in Ant. 5. The symmetric relation is expressed as follows:

$$\gamma_r(\theta_{r_k}) - \gamma_s(\theta_{s_k}) = \sum_{n=0}^N \{a_{n,r} \cos(n \times \theta_{r_k} \times \pi/180) + b_{n,r} \sin(n \times \theta_{r_k} \times \pi/180)\} - \sum_{n=0}^N \{a_{n,s} \cos(n \times \theta_{s_k} \times \pi/180) + b_{n,s} \sin(n \times \theta_{s_k} \times \pi/180)\} = 0, \quad (6)$$

when $r = 1, 5$, and $s = r$ and when $r = 2, 3, 4$ and $s = 10 - r$. For $\theta_{r_k} = k - 181$ ($k = 1, 2, \dots, 360$), θ_{s_k} has the same remainder as $-\theta_{r_k}$ divided by 360, $\theta_{s_k} \equiv (-\theta_{r_k}) \pmod{360}$, and $-180 \leq \theta_{s_k} < 180$. The operator mod 360 denotes the remainder operator divided by 360.

Considering Equations (4)–(6), the equation group is shown in Equations (7) and (8). \mathbf{H} is the observation matrix; \mathbf{X} is the solution matrix consisting of Fourier coefficients and array calibration coefficients $\beta_{21}, \dots, \beta_{81}$; and \mathbf{Y} is a matrix consisting of $\mathbf{0}$ submatrices and sampling submatrices derived from the source calibration signals $\phi_{21} - \alpha_{21}, \dots, \phi_{81} - \alpha_{81}$.

$$\mathbf{HX} = \mathbf{Y} \quad (7)$$

$$\begin{bmatrix}
 -\mathbf{A} & \mathbf{B} & \mathbf{0} \\
 -\mathbf{A} & \mathbf{0} & \mathbf{B} & \mathbf{0} & \mathbf{0} & \mathbf{0} & \mathbf{0} & \mathbf{0} & \mathbf{0} \\
 \vdots & & \dots & & \ddots & & \dots & & \vdots \\
 -\mathbf{A} & \mathbf{0} & \mathbf{B} \\
 \mathbf{C} & \mathbf{0} \\
 \mathbf{0} & \mathbf{D} & \mathbf{0} \\
 \mathbf{0} & \mathbf{0} & \mathbf{D} & \mathbf{0} & \mathbf{0} & \mathbf{0} & \mathbf{0} & \mathbf{0} & \mathbf{0} \\
 \vdots & & \dots & & \ddots & & \dots & & \vdots \\
 \mathbf{0} & \mathbf{D} \\
 \mathbf{F}_1 & \mathbf{0} \\
 \mathbf{0} & \mathbf{F} & \mathbf{0} & \mathbf{0} & \mathbf{0} & \mathbf{0} & \mathbf{0} & \mathbf{0} & -\mathbf{G} \\
 \mathbf{0} & \mathbf{0} & \mathbf{F} & \mathbf{0} & \mathbf{0} & \mathbf{0} & -\mathbf{G} & \mathbf{0} & \mathbf{0} \\
 \mathbf{0} & \mathbf{0} & \mathbf{0} & \mathbf{F} & \mathbf{0} & -\mathbf{G} & \mathbf{0} & \mathbf{0} & \mathbf{0} \\
 \mathbf{0} & \mathbf{0} & \mathbf{0} & \mathbf{0} & \mathbf{F}_5 & \mathbf{0} & \mathbf{0} & \mathbf{0} & \mathbf{0}
 \end{bmatrix}
 \begin{bmatrix}
 a_{0,1} \\
 a_{1,1} \\
 b_{1,1} \\
 \vdots \\
 a_{N,1} \\
 b_{N,1} \\
 \beta_{21} \\
 a_{0,2} \\
 \vdots \\
 b_{N,2} \\
 \vdots \\
 \beta_{81} \\
 a_{0,8} \\
 \vdots \\
 b_{N,8}
 \end{bmatrix}
 =
 \begin{bmatrix}
 \phi_{21} - \alpha_{21} \\
 \phi_{31} - \alpha_{31} \\
 \vdots \\
 \phi_{81} - \alpha_{81} \\
 \mathbf{0} \\
 \mathbf{0}
 \end{bmatrix}, \tag{8}$$

where the submatrices **A** and **B** consisting of Fourier basis functions have the sizes $276 \times (2 \times N + 1)$ and $276 \times (2 \times N + 2)$, corresponding to Equation (4); similarly, **C** and **D** are $\lfloor 360/N_{Interval} \rfloor \times (2 \times N + 1)$ and $\lfloor 360/N_{Interval} \rfloor \times (2 \times N + 2)$ matrices, corresponding to Equation (5); **F**₁ is a matrix of size $360 \times (2 \times N + 1)$, and **F**, **F**₅ and **G** are $360 \times (2 \times N + 2)$ matrices, corresponding to Equation (6).

H is written as **H**_{*p*×*q*}, where $p = 276 \times 7 + \lfloor 360/N_{Interval} \rfloor \times 8 + 360 \times 5 = 4020$ ($N_{Interval} = 10$) is the row size of matrix **H** and $q = (2 \times N + 1) + (2 \times N + 2) \times 7 = 303$ ($N = 18$) is the column size of **H**. Note that the details of $N_{Interval} = 10$, as the angular interval, and $N = 18$, as the total number of Fourier series, are discussed in the Appendix B.

The rank of **H** is labeled $rank(\mathbf{H}) = q$, where $q < p$. The equation group is a typical overdetermined equation group (the number of equations is larger than the number of unknown solutions), which is treated as a least-squares problem. After the process of singular value decomposition (SVD), **H**_{*p*×*q*} can be represented as

$$\mathbf{H}_{p \times q} = \mathbf{U}_{p \times p} \mathbf{S}_{p \times q} \mathbf{V}_{q \times q}^T = \mathbf{U}_{p \times p} \begin{bmatrix} \mathbf{\Sigma}_{q \times q} \\ \mathbf{0}_{(p-q) \times q} \end{bmatrix} \mathbf{V}_{q \times q}^T \tag{9}$$

U_{*p*×*p*} and **V**_{*q*×*q*} are two orthogonal matrices, and **Σ**_{*q*×*q*} is a diagonal matrix. **H**[†] is the generalized inverse matrix or Moore–Penrose pseudoinverse matrix of **H** [50],

$$\mathbf{H}^\dagger = \mathbf{V}_{q \times q} \mathbf{\Sigma}_{q \times q}^{-1} \mathbf{U}_{1 p \times q}^T \tag{10}$$

where **U**_{1*p*×*q*} is the first *q* column of **U**_{*p*×*p*}. The least-squares solution to this equation group is expressed as

$$\hat{\mathbf{X}} = \arg \min_{\mathbf{X}} \|\mathbf{H}\mathbf{X} - \mathbf{Y}\|_2^2 = \mathbf{H}^\dagger \mathbf{Y}. \tag{11}$$

The phase patterns $\gamma_m(\theta)$ versus the DOA bearing θ in Cartesian coordinates are shown in Figure 9a. In addition, $e^{\gamma_m(\theta)}$ is an alternative style in polar coordinates in Figure 9b.

Equation (2) is similar to Equation (1), so the solution to the amplitude patterns is also a least-squares problem. The same study is repeated, and C_{dB_m} is transformed to $C_m(\theta) = 10^{\frac{C_{dB_m}(\theta)}{20}}$. The amplitude patterns $C_m(\theta)$ in Cartesian and polar coordinates are shown in Figure 10a,b, respectively.

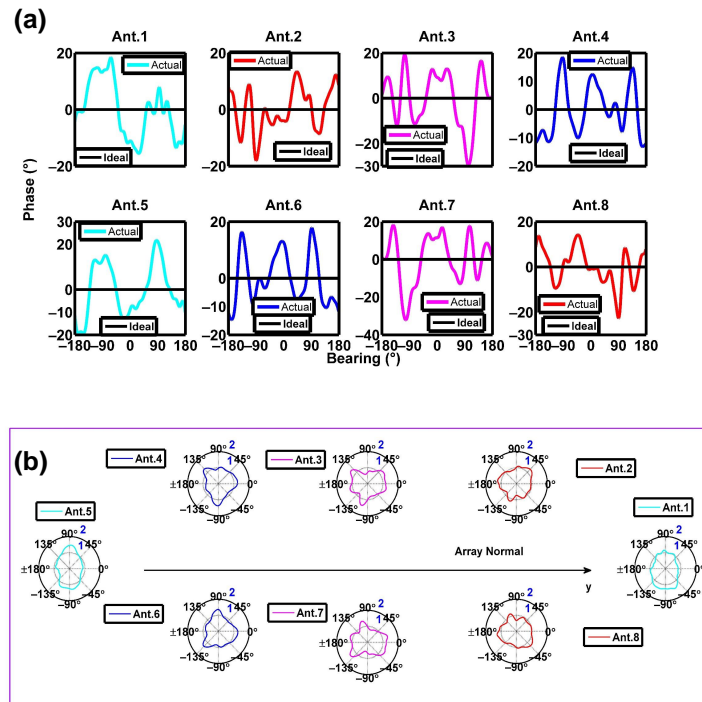


Figure 9. Phase patterns of the eight antennas: (a) $\gamma_m(\theta)$ in Cartesian coordinates, where “Ideal” and “Actual” denote uncalibrated and calibrated antenna patterns, respectively; (b) $e^{\gamma_m(\theta)}$ in polar coordinates. Each bearing of $-180^\circ \leq \theta < 180^\circ$ in this figure indicates degrees counterclockwise from the y axis.

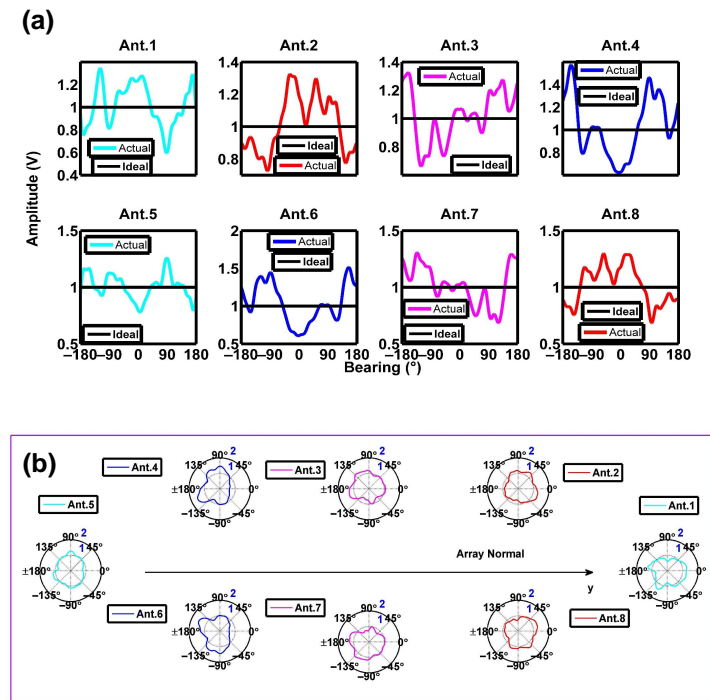


Figure 10. Amplitude patterns of the eight antennas: (a) $C_m(\theta)$ in Cartesian coordinates; (b) $C_m(\theta)$ in polar coordinates.

3. Results

For shore-based HF radars, there are several methods for measuring antenna patterns [25,29,51]. The Euclidean distance is used to quantify the difference between the complex antenna pattern vectors at each bearing from the AIS method [25] (or the aerial drone method [29]) and the traditional transponder method [51]. Because conventional transponder measurements have not been conducted for platform-mounted HF radars, we intend to validate the platform-mounted HF radar patterns depending on the inversion results.

The calibrated patterns and the channel calibration coefficients are both calculated in this study, which is called complete calibration or standard calibration. First, we can check the validity of the channel calibration coefficients. Next, we can compare the results for complete calibration with those for incomplete calibration (the channel calibration coefficients and uncalibrated patterns are considered). This type of comparison can evaluate the sole influence of calibrated antenna patterns in the complete calibration system. Consequently, we devoted substantial effort to studying how to best adopt these channel calibration coefficients and calibrated patterns in the calibration of the inversion results. The results can be verified based on the target DOA, the radial current, and the bearing offset.

Note that the DOA bearing is the most convincing validation source because it is directly affected by the channel calibration coefficients and antenna patterns based on the MUSIC algorithm. In addition, some correctly determined radial velocities will be placed into incorrect bearing sectors because of the incorrect DOA bearing, and thus, the radial current is the secondary validation source. In addition, we attempt to calculate the bearing offset using root-mean-square error (RMSE) and correlation coefficient (CC) between acoustic Doppler current profiler (ADCP)-derived radial currents and platform-mounted HF radar radial velocities within a fixed range (ADCP deployed) and for all angles [52]. The bearing offset reflects the bearing angle bias between the platform-mounted HF radar measurement and the ADCP measurement.

3.1. DOA

Before validating the calibrated antenna patterns, we can check the validity of the channel calibration coefficients with respect to the DoSA DOA bearing. The DoSA land station, for which the range and bearing are definite, can offer a stable and robust radio signal. Under these circumstances, we can consider DoSA as a “target” to verify our platform-mounted HF radar patterns. The DoSA actual bearing $\theta_{Actual_{DoSA}} = -97.3^\circ$, which is expressed as the angle clockwise from true north to the DoSA direction, can be calculated from the latitude and longitude of the ship site, DoSA radar site, and the radius of the Earth.

First, the MUSIC algorithm can be used to estimate the DOA bearing $\theta_{CW_{DoSA}}$ for every 5 min of the Doppler CIT without any calibration (neither the array calibration coefficients nor the calibrated patterns are considered). DOA curves are drawn from the DoSA radar site’s calculated DOA from approximately 24 h of data and the actual bearing starting at 1300 UTC+8 25 December 2016 and ending at 1300 UTC+8 26 December 2016 (Figure 11a). The DOA results are terribly poor without any calibration.

Next, the MUSIC algorithm can use either the uncalibrated or calibrated patterns to estimate the DOA bearing $\theta_{CW_{DoSA}}$ for the case considering the channel calibration coefficients. DOA curves before and after the pattern corrections are drawn from the DoSA radar site’s calculated DOA from approximately 24 h of data and the actual bearing (Figure 11b). From Figure 11a,b, the DOA bearing estimation improved dramatically after the channel calibration. These results prove that the channel calibration coefficients are valid.

The statistical values shown in Table 2 represent both the calibrated and uncalibrated patterns. The five statistical values improved after pattern corrections, especially in terms of the standard deviation, indicating that the DOA estimation is more accurate with the calibrated patterns than the uncalibrated patterns for the DoSA radar site.

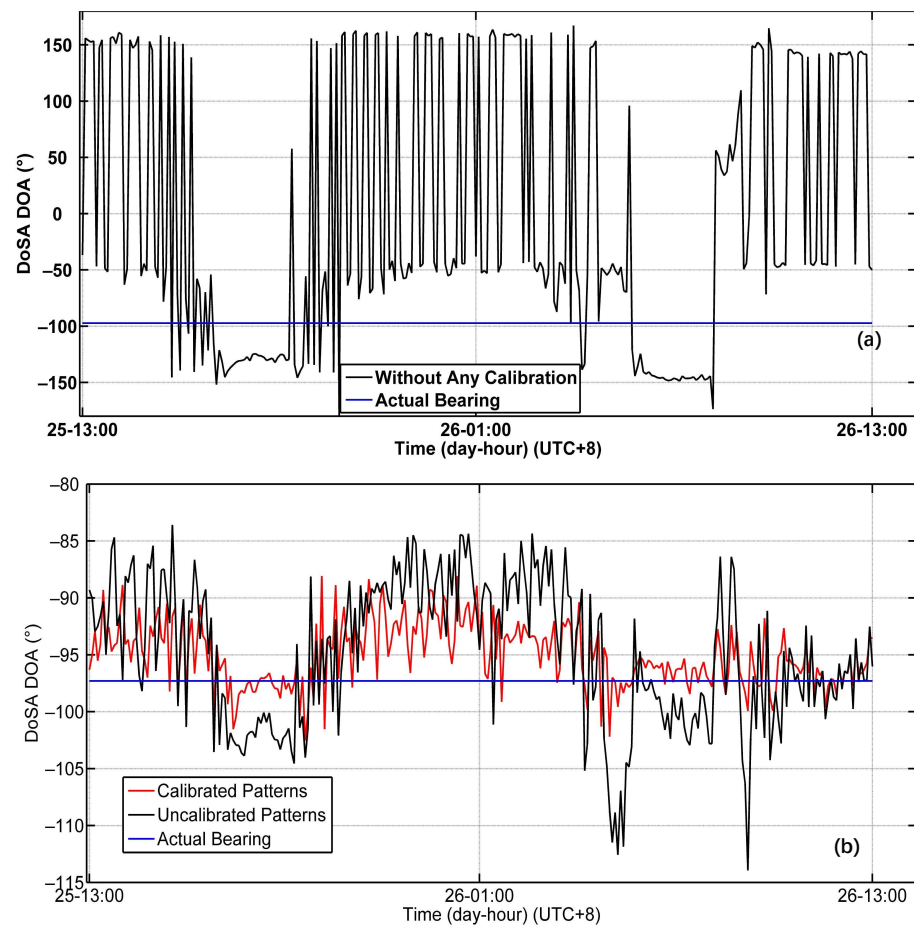


Figure 11. From 1300 UTC+8 25 December 2016 to 1300 UTC+8 26 December 2016: (a) DoSA DOA without any calibration (black line) compared with the actual DoSA bearing (blue line); (b) DoSA DOA before pattern corrections (black line) and after pattern corrections (red line) compared with the actual DoSA bearing (blue line).

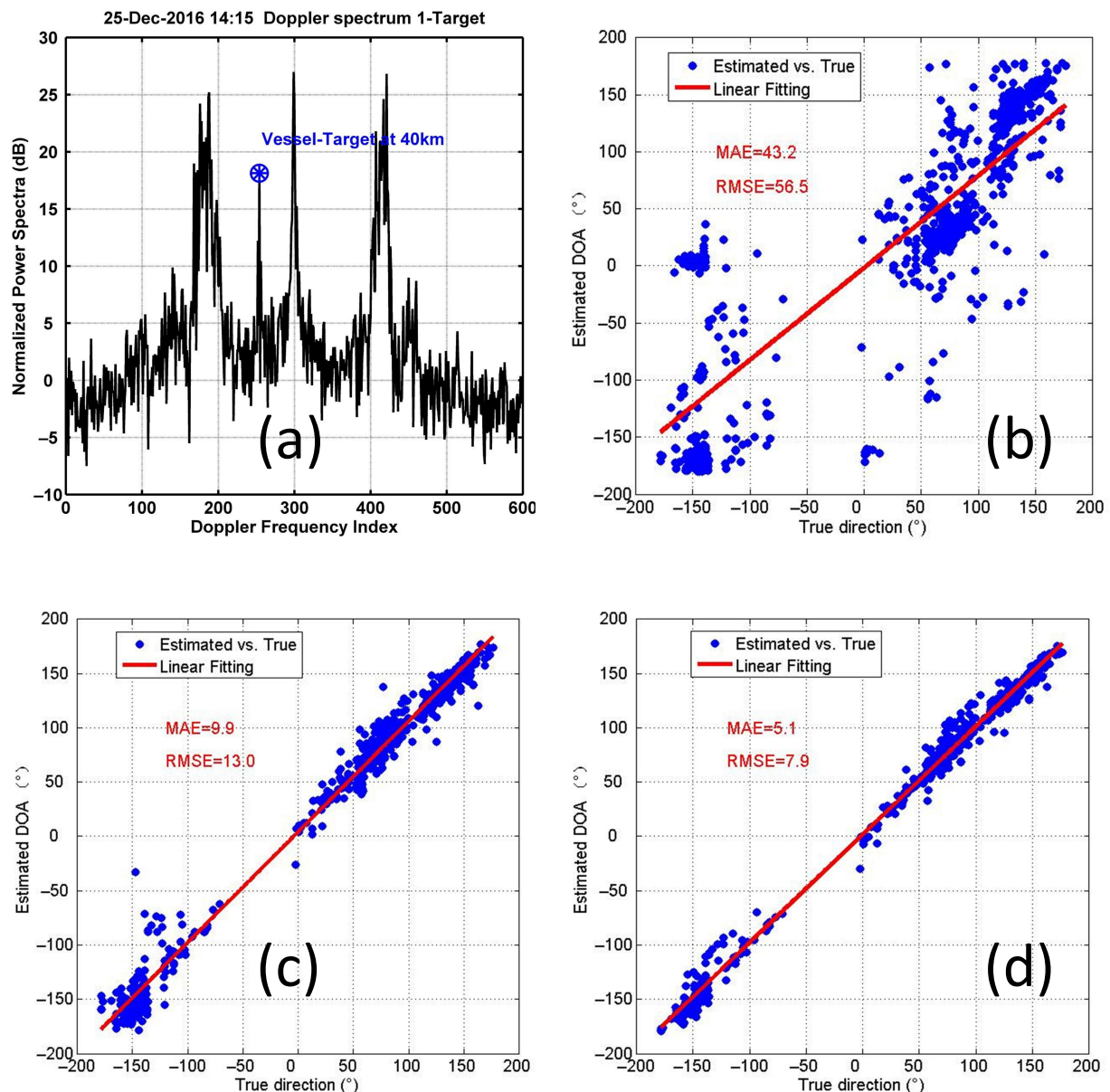
Table 2. DoSA DOA statistics using the uncalibrated and calibrated patterns

DoSA DOA ($\theta_{CW_{DoSA}}$)	Mean (°)	Std. (°)	Max. (°)	Min. (°)	Med. (°)
Calibrated Channels and Uncalibrated Patterns	−95.0	6.3	−83.6	−113.9	−94.1
Calibrated Channels and Calibrated Patterns	−95.1	2.8	−88.1	−102.5	−95.5
Actual DoSA bearing ($\theta_{Actual_{DoSA}}$)			−97.3		

On the other hand, the vessel targets corresponding to the AIS information can be detected with the platform-mounted HF radar (see an example in Figure 12a). The estimated 725 vessel-target DOAs in 24 h can reflect the validity of the channel calibration coefficients and calibrated patterns (see Figure 12b–d). The mean absolute error (MAE) and RMSE can be used to evaluate the validity. The RMSE and MAE are improved by 43.5° and 33.3° after channel calibration, respectively. Furthermore, the RMSE and MAE are improved by 5.1° and 4.8° after channel calibration and pattern calibration, respectively. Table 3 shows the technical specifications for convenience.

Table 3. Estimated vessel-target DOAs compared with the true vessel-target directions without any calibration, after channel calibration, and after pattern calibration

725 Vessel-Target DOAs vs. True Directions	RMSE (°)	MAE (°)
Uncalibrated Channel and Uncalibrated Patterns	56.5	43.2
Calibrated Channels and Uncalibrated Patterns	13.0	9.9
Calibrated Channels and Calibrated Patterns	7.9	5.1

**Figure 12.** From 1300 UTC+8 25 December 2016 to 1300 UTC+8 26 December 2016: (a) an example of a vessel target in the range of 40 km detected by the platform-mounted HF radar and denoted by a blue asterisk embedded in a circle in the Doppler spectrum (Ant. 8); (b) estimated 725 vessel-target DOAs (clockwise from true north to the vessel target) compared with the true directions without any calibration; (c) estimated 725 vessel-target DOAs after channel calibration; (d) estimated 725 vessel-target DOAs after channel calibration and pattern calibration.

3.2. Radial Current and Bearing Offset

ADCPs are very common in situ instruments used to validate HF radar currents. ADCP-radial currents can provide the standard to validate the calibrated patterns. The ADCP called “Aquadopp Profiler” manufactured by Nortek company was integrated into a 10 m discus “buoy” (abbreviated as “B” and located at 23°37′47″N, 118°12′1″E, see Figure 13). There was a technical problem with the ADCP compass, and thus, the ADCP data are not used.

However, due to the complexity of the platform motion and imperfection of the motion-compensation technique for the platform-mounted HF radar, the shore-based radar systems that have been calibrated are more developed and reliable systems than the platform-mounted HF radar system. Hence, the data from shore-based HF radar systems can be considered the reference data for validating the calibrated antenna patterns for the platform-mounted HF radar. Accordingly, the radial current $V_{Radial_{ship}}$ measured by the ship radar site (for the case using the uncalibrated (black line) and calibrated patterns (red line)) is compared with the radial projection $V_{Prj_{shore}}$ (blue line) of the total vector current $V_{Total_{shore}}$ produced by the shore radar sites (see Figure 14a).

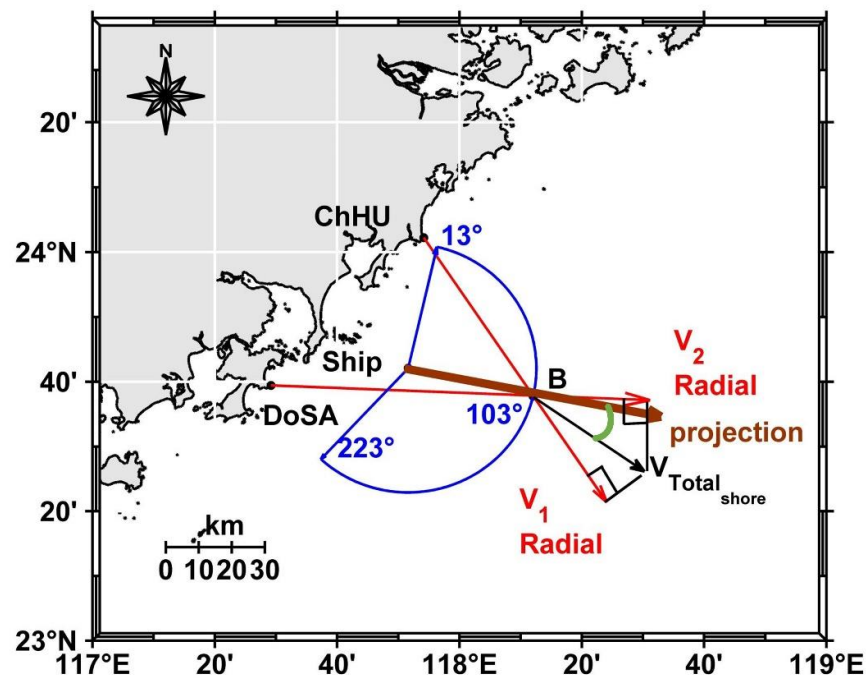


Figure 13. Total vector currents: $V_{Total_{shore}}$ (black line) calculated from two radial currents V_1 (red line) and V_2 (red line) by the two shore radar sites; the carmine line (from the ship site to ‘B’) denotes the radial projection of $V_{Total_{shore}}$; the green angle denotes the projection angle.

The total vector current $V_{Total_{shore}}$ produced by the shore radar sites is calculated by combining the two radial currents measured by the two shore sites, as shown in Figure 13. α_1 is the direction of V_1 , α_2 is the direction of V_2 , and $\alpha_{Total_{shore}}$ is the direction of total vector current $V_{Total_{shore}}$. The formulas are expressed as follows in Equation (12).

$$\begin{cases} V_1 = V_{Total_{shore}} \cos(\alpha_{Total_{shore}} - \alpha_1) \\ V_2 = V_{Total_{shore}} \cos(\alpha_{Total_{shore}} - \alpha_2) \end{cases} \quad (12)$$

At ‘B’, the radial currents measured by ship site $V_{Radial_{ship}}$ (uncalibrated patterns versus calibrated patterns) can be compared with the radial projection $V_{Prj_{shore}}$ and the projection

along radial direction α_{prj} (e.g., the crimson line from the ship site to 'B' in Figure 13). The conversion is described as follows:

$$V_{Prj_{shore}} = V_{Total_{shore}} \cos(\alpha_{Total_{shore}} - \alpha_{prj}), \quad (13)$$

where the green angle denotes $\alpha_{Total_{shore}} - \alpha_{prj}$ in Figure 13.

The raw radial speeds are smoothed by means of a five-point moving average filter. The RMSE and CC can be used to assess and evaluate the performance of the amendment process. At 'B', the RMSE is reduced by 2.75 cm s^{-1} , and the CC is increased by 0.18 after using the calibrated patterns from Figure 14a. The radial speed correlation between the shore and ship sites after using the calibrated patterns has been improved.

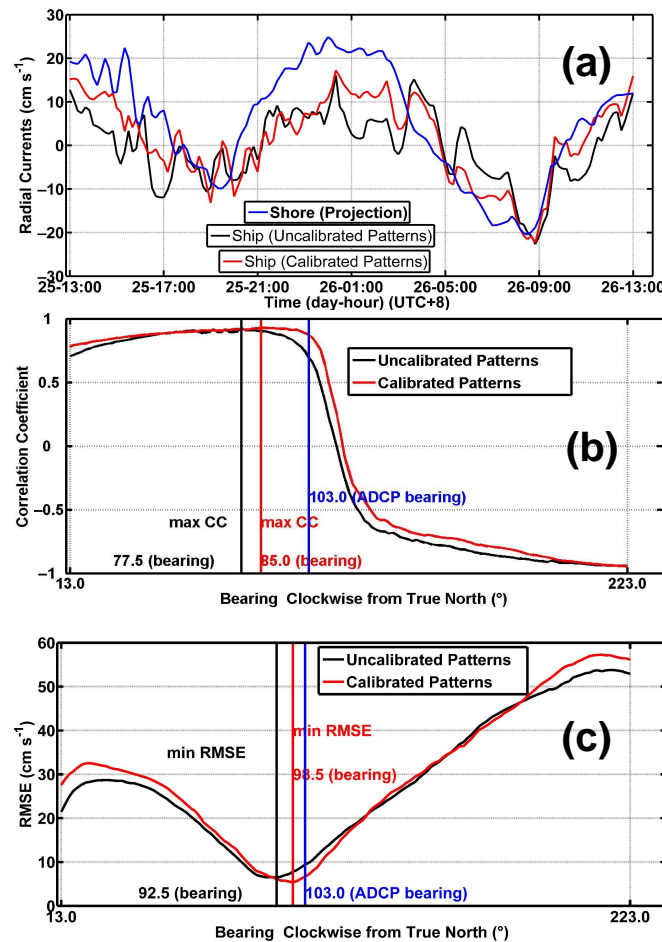


Figure 14. Point 'B' from 1300 UTC+8 25 December 2016 to 1300 UTC+8 26 December 2016: (a) radial currents detected by the ship radar site (using the uncalibrated (black line) and the calibrated patterns (red line)) compared with the radial projection (blue line) of total vector currents produced by the shore radar sites; (b) CCs at a fixed range passing through point 'B' before pattern corrections (black line) and after pattern corrections (red line); (c) RMSEs at a fixed range passing through point 'B' before pattern corrections (black line) and after pattern corrections (red line).

We intended to estimate the bearing offset with a given range cell following the procedures described in [52] using the radial projection $V_{Prj_{shore}}$ of the total vector current $V_{Total_{shore}}$ instead of the ADCP-derived radial current because of the lack of ADCP direction data.

For a given range to the platform-mounted radar site, all radial velocities are sampled for the bearing angle sectors from 13° to 223° (clockwise from true north in Figure 13) at a resolution of 1.5° and then correlated with $V_{Prj_{shore}}$ at 'B'. Thus, many RMSEs and CCs have

been calculated at the bearing sectors from 13° to 223° . The CC and RMSE bearing offsets are thus expressed as

$$\begin{cases} \Delta\theta_{CC} = \theta_B - \theta_{max} \\ \Delta\theta_{RMSE} = \theta_B - \theta_{min} \end{cases} \quad (14)$$

where $\theta_B = 103^\circ$ is the bearing angle with respect to 'B', θ_{max} is the angle with maximum CC, and θ_{min} is the angle with minimum RMSE. From Figure 14b,c, the bearing offsets $\Delta\theta_{CC} = 103 - 77.5 = 25.5^\circ$ and $\Delta\theta_{RMSE} = 103 - 92.5 = 10.5^\circ$ when the uncalibrated patterns are used; on the other hand, $\Delta\theta_{CC} = 103 - 85 = 18^\circ$ and $\Delta\theta_{RMSE} = 103 - 98.5 = 4.5^\circ$ when the calibrated patterns are used. The CC and RMSE bearing offsets are improved by 7.5° and 6° after pattern corrections, respectively. Table 4 shows the technical specification in detail for convenience.

Table 4. Comparison statistics with respect to the shore using the uncalibrated and calibrated patterns at 'B'.

Ship ($V_{Radial_{ship}}$)	Shore ($V_{Prj_{shore}}$)		Shore (Bearing Offset)	
	RMSE (cm s^{-1})	CC	$\Delta\theta_{RMSE}$ ($^\circ$)	$\Delta\theta_{CC}$ ($^\circ$)
Calibrated Channels and Uncalibrated Patterns	9.40	0.69	10.5	25.5
Calibrated Channels and Calibrated Patterns	6.65	0.87	4.5	18

4. Discussion

In the present study, the calibrated patterns, which can be considered the least-squares solutions close to the uncalibrated patterns based on the overdetermined system consisting of observed values and theoretical constraints, and the channel calibration coefficients are obtained. The suggested scheme is a type of model-fitting and real-time calibration technique. The results validated the channel calibration coefficients and calibrated antenna patterns for target DOA estimation and surface current measurement. The antenna pattern calibration can result in more accurate DOA estimation in a complete calibration system. The following topics are analyzed in regard to this scheme:

First, the values observed account for a considerable part of the overdetermined system. The yaw angles (a total of 276°) occupied approximately 77% of the 360° space and, hence, could not cover the omni-directional range in this experiment. Their probabilities of emergence depend on the sea state (i.e., ocean surface currents, winds, and waves). As the yaw angles occupy more of the 360° space, the estimation of the antenna patterns becomes more accurate. Moreover, the least-squares solutions to the antenna patterns will be studied more under other constraints.

Second, this experiment (i.e., wherein the rotating ship radar received the radio signal from the shore-based radar site) appeared to be an inverted one compared with the conventional transponder experiment (i.e., wherein the shore-based radar site received the radio signal from the transponder on a boat).

Third, the superstructures in the ship and iron body of the ship could cause antenna pattern distortions. Moreover, the antenna patterns on the ship can be simulated and predicted by means of computational electromagnetics such as the method-of-moments (MOM) [53–55], which is a good auxiliary validation method.

5. Conclusions

In light of the discussion above, the suggested scheme seems to be a cost-effective way to estimate the channel calibration coefficients and antenna patterns for platform-mounted HF radars. The platform motion should be eliminated in the signal processing for HF radars on a floating platform. In contrast, this study aims to incorporate the influence of the moving antenna array due to platform motion into HF radar data processing. Finally, the scheme could potentially be applied to the shore-based HF radar if a supplementary rotary turntable were configured [56].

We can achieve better DOA estimation by calibrating the platform-mounted HF radar. Furthermore, reliable DOA estimation for platform-mounted HF radar is a key technology not only for ocean current measurement but also for ocean wind and wave measurements. Consequently, ocean wind and wave measurements would become available for further research.

Additionally, because the influence of other five-DOF motion (sway translation, surge translation, heave translation, roll rotation, and pitch rotation) is ignored, we only consider specific anchored platform-mounted HF radars with yaw rotation under a low sea state. Under a high sea state and a more comprehensive analysis, more studies about the influence of other five-DOF motion are needed. Finally, compared with anchored platform-mounted HF radar, forward movement will be considered in the calibration of sailing platform-mounted HF radar in the future. All of these are useful and can fully develop the platform-mounted HF radar's application potential.

Author Contributions: Conceptualization, X.W.; methodology, B.W. and X.W.; software, X.W.; validation, B.W., X.Y., L.Z., and L.W.; formal analysis, X.W. and B.W.; investigation, B.W.; resources, X.W.; data curation, X.Y.; writing—original draft preparing, B.W.; writing—review and editing, B.W. and X.Y.; visualization, B.W.; supervision, B.W.; project administration, X.W.; funding acquisition, X.W. All authors have read and agreed to the published version of the manuscript.

Funding: This work was supported by the National Key R & D Program of China under Grant 2016YFC1401100.

Data Availability Statement: The data presented in this study are available from the corresponding author on reasonable request.

Acknowledgments: The authors thank the technicians from China Precise Ocean Detection Technology Co., Ltd. (No. 21 Qingdao Road, Yichang City, Hubei Province, China) for installing the radar equipment on the ship platform. In addition, the authors thank the anonymous reviewers for their valuable and constructive suggestions that helped improve this manuscript.

Conflicts of Interest: The authors declare no conflicts of interest.

Appendix A. Influence of Six-DOF Platform Motion

The easterly speed and northerly speed are defined as the easterly and northerly components of the translational motion speeds in Figure 4d. The easterly and northerly speeds are measured instead of the sway and surge motion. The roll angle is defined as the clockwise angle with respect to the barge's longitudinal axis (y axis) (see Figure 4a), while the pitch angle is defined as the clockwise angle with respect to the transversal axis (x axis) (see Figure 4b). In addition, the upward speed is measured instead of the heave motion. Because the electromagnetic field distribution in the vertical direction is assumed to be the same everywhere and the radar transmits vertically polarized waves, the influence of heave motion (upward speed) in the Doppler spectrum is ignored.

If the easterly and northerly speeds were kept constant in a Doppler CIT, the Doppler frequency would experience a shift and the Doppler spectra would suffer spreading based on the Doppler coherent integration effect of the additional phase due to the constant ship velocity. This phenomenon and theory were described from the sailing shipborne HF radar experiment conducted by [57,58]. Unlike the sailing shipborne HF radar experiment, the easterly and northerly speeds (time span 1 s) of the anchored ship-mounted HF radar experiment cannot maintain a constant sailing speed (see Figure A1a,b). Accordingly, the impact of the easterly and northerly speeds in the Doppler spectrum was ignored.

Furthermore, the ranges of the variation in the roll and pitch motion (see Figure A1c,d) were much less than that in the yaw motion. In this study, we consider the influence of the moving antenna array focused on the dominant yaw rotation.

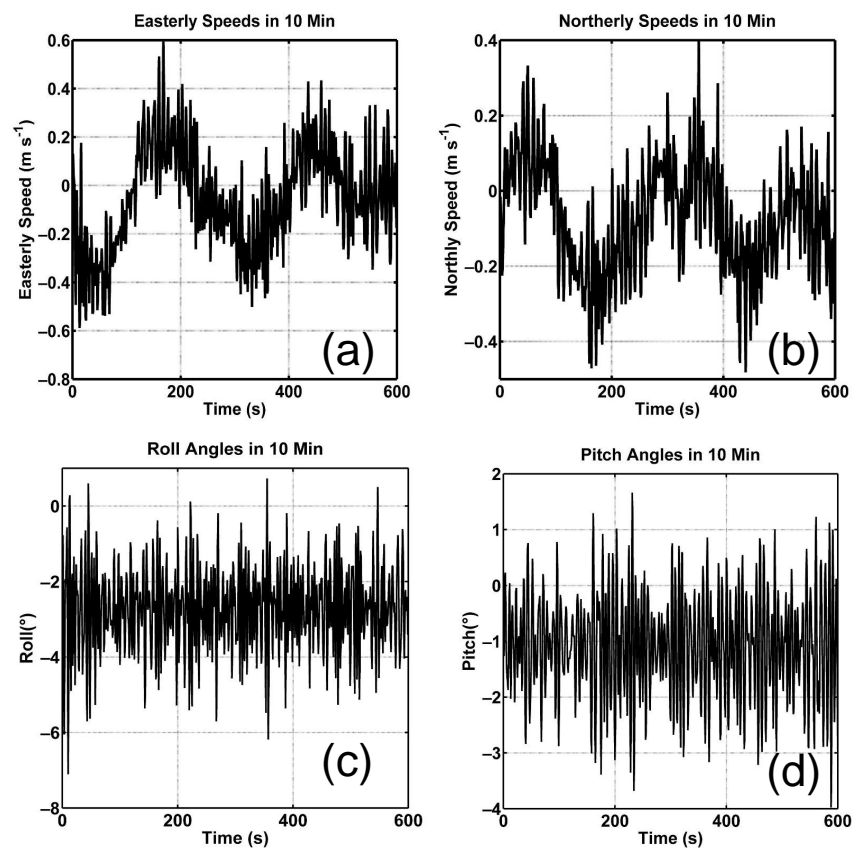


Figure A1. In the first 10 min (time span 1 s): (a) easterly speeds, (b) northerly speeds, (c) roll angles, and (d) pitch angles.

Appendix B. Analysis of the Least-Squares Solution

First, the estimated phase pattern represented by the Fourier series approaches the real phase patterns as the number N increases. This is related to the convergence of the Fourier series. The sensitivity analysis of phase patterns versus N is shown in Figure A2a. When $N \geq 18$, the phase pattern value approaches a constant value. Accordingly, $N = 18$ is a reasonable choice.

Second, the additional constraint of the actual patterns (i.e., calibrated patterns) close to the ideal patterns (i.e., uncalibrated patterns) should be discussed (see Figure A2b). If $N_{interval} > 35$, the solution cannot be found because the number of constraints in the overdetermined system is not sufficient ($\lfloor 360/N_{interval} \rfloor$ is small). We have chosen many angular intervals between 1° and 35° to compare the DoSA DOA with the actual DoSA bearing as well as the radial currents with those measured by the shore radar sites. The comparison results are the best when the angular interval $N_{interval} = 10$ is used. Accordingly, $N_{interval} = 10$ is a suitable option.

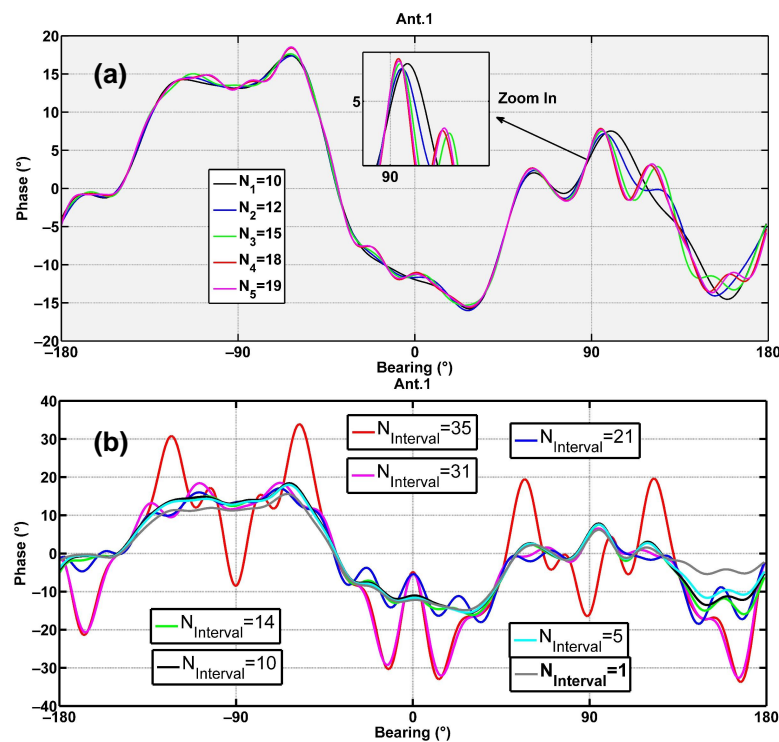


Figure A2. Phase pattern of Ant. 1: (a) versus the total number N of Fourier series; (b) versus the angular interval $N_{interval}$.

References

1. Crombie, D.D. Doppler spectrum of sea echo at 13.56 Mc./s. *Nature* **1955**, *175*, 681–682. [\[CrossRef\]](#)
2. Barrick, D.; Evans, M.; Weber, B. Ocean surface currents mapped by radar. In Proceedings of the 1978 IEEE First Working Conference on Current Measurement, Newark, DE, USA, 11–13 January 1978; Volume 1, pp. 59–65.
3. Lipa, B.; Barrick, D. Least-squares methods for the extraction of surface currents from CODAR crossed-loop data: Application at ARSLOE. *IEEE J. Ocean. Eng.* **1983**, *8*, 226–253. [\[CrossRef\]](#)
4. Lipa, B.; Barrick, D.E.; Diposaptono, S.; Isaacson, J.; Jena, B.K.; Nyden, B.; Rajesh, K.; Kumar, T.S. High Frequency (HF) Radar Detection of the Weak 2012 Indonesian Tsunamis. *Remote Sens.* **2012**, *4*, 2944–2956. [\[CrossRef\]](#)
5. Lipa, B.; Isaacson, J.; Nyden, B.; Barrick, D.E. Tsunami Arrival Detection with High Frequency (HF) Radar. *Remote Sens.* **2012**, *4*, 1448–1461. [\[CrossRef\]](#)
6. Guérin, C.A.; Grilli, S.T.; Moran, P.; Grilli, A.R.; Insua, T.L. Tsunami detection by high-frequency radar in British Columbia: performance assessment of the time-correlation algorithm for synthetic and real events. *Ocean Dyn.* **2018**, *68*, 423–438. [\[CrossRef\]](#)
7. Lipa, B.; Barrick, D.; Isaacson, J. Evaluating hf coastal radar site performance for tsunami warning. *Remote Sens.* **2019**, *11*, 2773. [\[CrossRef\]](#)
8. Abascal, A.J.; Castanedo, S.; Fernandez, V.; Ferrer, M.I.; Medina, R. Oil spill trajectory forecasting and backtracking using surface currents from high-frequency (HF) radar technology. In Proceedings of the OCEANS 2011 IEEE—Spain, Santander, Spain, 6–9 June 2011; pp. 1–8.
9. Bellomo, L.; Griffo, A.; Cosoli, S.; Falco, P.; Gerin, R.; Iermano, I.; Kalampokis, A.; Kokkini, Z.; Lana, A.; Magaldi, M.; et al. Toward an integrated HF radar network in the Mediterranean Sea to improve search and rescue and oil spill response: the TOSCA project experience. *J. Oper. Oceanogr.* **2015**, *8*, 95–107. [\[CrossRef\]](#)
10. Abascal, A.J.; Sanchez, J.; Chiri, H.; Ferrer, M.I.; Cárdenas, M.; Gallego, A.; Castanedo, S.; Medina, R.; Alonso-Martirena, A.; Berx, B.; et al. Operational oil spill trajectory modelling using HF radar currents: A northwest European continental shelf case study. *Mar. Pollut. Bull.* **2017**, *119*, 336–350. [\[CrossRef\]](#)
11. Choi, J.W.; Song, K.M.; Choi, J.Y. Accuracy improvement of particle tracking model using 2-D current measurement (HF-radar) data. *J. Coast. Res.* **2019**, *91*, 251–255. [\[CrossRef\]](#)
12. Schmidt, R. Multiple emitter location and signal parameter estimation. *IEEE Trans. Antennas Propag.* **1986**, *34*, 276–280. [\[CrossRef\]](#)
13. Barrick, D.E.; Lipa, B.J. Evolution of bearing determination in HF current mapping radars. *Oceanography* **1997**, *10*, 72–75. [\[CrossRef\]](#)
14. Laws, K.E.; Fernandez, D.M.; Paduan, J.D. Simulation-based evaluations of HF radar ocean current algorithms. *IEEE J. Ocean. Eng.* **2000**, *25*, 481–491. [\[CrossRef\]](#)

15. Yang, S.; Ke, H.; Wu, X.; Tian, J.; Hou, J. HF radar ocean current algorithm based on MUSIC and the validation experiments. *IEEE J. Ocean. Eng.* **2005**, *30*, 601–618. [[CrossRef](#)]
16. Emery, B.; Kirincich, A.; Washburn, L. Direction Finding and Likelihood Ratio Detection for Oceanographic HF Radars. *J. Atmos. Ocean. Technol.* **2022**, *39*, 223–235. [[CrossRef](#)]
17. Barrick, D.; Lipa, B. Correcting for distorted antenna patterns in CODAR ocean surface measurements. *IEEE J. Ocean. Eng.* **1986**, *11*, 304–309. [[CrossRef](#)]
18. Laws, K.; Paduan, J.D.; Vesecky, J. Estimation and assessment of errors related to antenna pattern distortion in CODAR SeaSonde high-frequency radar ocean current measurements. *J. Atmos. Ocean. Technol.* **2010**, *27*, 1029–1043. [[CrossRef](#)]
19. Emery, B.; Washburn, L. Uncertainty estimates for SeaSonde HF radar ocean current observations. *J. Atmos. Ocean. Technol.* **2019**, *36*, 231–247. [[CrossRef](#)]
20. Capodici, F.; Cosoli, S.; Ciruolo, G.; Nasello, C.; Maltese, A.; Poulain, P.; Drago, A.; Azzopardi, J.; Gauci, A. Validation of HF radar sea surface currents in the Malta-Sicily Channel. *Remote Sens. Environ.* **2019**, *225*, 65–76. [[CrossRef](#)]
21. Xiongbing, W.; Feng, C.; Zijie, Y.; Hengyu, K. Broad Beam HFSWR Array Calibration Using Sea Echoes. In Proceedings of the 2006 CIE International Conference on Radar, Shanghai, China, 16–19 October 2006; pp. 1–3.
22. Fernandez, D.M.; Vesecky, J.F.; Teague, C. Calibration of HF radar systems with ships of opportunity. In Proceedings of the IGARSS 2003: IEEE International Geoscience and Remote Sensing Symposium, International Geoscience and Remote Sensing Symposium, Toulouse, France, 21–25 July 2003; Volumes I–VII, pp. 4271–4273.
23. Fernandez, D.; Vesecky, J.; Teague, C. Phase Corrections of Small-Loop HF Radar System Receive Arrays With Ships of Opportunity. *IEEE J. Ocean. Eng.* **2006**, *31*, 919–921. [[CrossRef](#)]
24. Flores-Vidal, X.; Flament, P.; Durazo, R.; Chavanne, C.; Gurgel, K.W. High-frequency radars: Beamforming calibrations using ships as reflectors. *J. Atmos. Ocean. Technol.* **2013**, *30*, 638–648. [[CrossRef](#)]
25. Emery, B.M.; Washburn, L.; Whelan, C.; Barrick, D.; Harlan, J. Measuring antenna patterns for ocean surface current HF radars with ships of opportunity. *J. Atmos. Ocean. Technol.* **2014**, *31*, 1564–1582. [[CrossRef](#)]
26. Chen, Z.; Zhang, L.; Zhao, C.; Li, J. Calibration and Evaluation of a Circular Antenna Array for HF Radar Based on AIS Information. *IEEE Geosci. Remote Sens. Lett.* **2019**, *17*, 988–992. [[CrossRef](#)]
27. Zhao, C.; zong Chen, Z.; Li, J.; Ding, F.; Huang, W.; gang Fan, L. Validation and Evaluation of a Ship Echo-Based Array Phase Manifold Calibration Method for HF Surface Wave Radar DOA Estimation and Current Measurement. *Remote Sens.* **2020**, *12*, 2761. [[CrossRef](#)]
28. Sun, H.; Ji, Y.; Li, M.M.; Wang, Y.; Niu, J. Phase array amplitude and phase correction for HFSWR based on AIS information. In Proceedings of the IET International Radar Conference (IET IRC 2020), Online, 4–6 November 2021.
29. Washburn, L.; Romero, E.; Johnson, C.; Emery, B.; Gotschalk, C. Measurement of Antenna Patterns for Oceanographic Radars Using Aerial Drones. *J. Atmos. Ocean. Technol.* **2017**, *34*, 971–981. [[CrossRef](#)]
30. Lipa, B.; Barrick, D.; Isaacson, J.; Lilleboe, P. CODAR wave measurements from a North Sea semisubmersible. *IEEE J. Ocean. Eng.* **1990**, *15*, 119–125. [[CrossRef](#)]
31. Peters, N.J.; Skop, R.A. Measurements of ocean surface currents from a moving ship using VHF radar. *J. Atmos. Ocean. Technol.* **1997**, *14*, 676–694. [[CrossRef](#)]
32. Gurgel, K.W.; Essen, H.H. On the performance of a shipborne current mapping HF radar. *IEEE J. Ocean. Eng.* **2000**, *25*, 183–191. [[CrossRef](#)]
33. Wang, Z.; Xie, J.; Ji, Z.; Quan, T. Remote sensing of surface currents with single shipborne high-frequency surface wave radar. *Ocean Dyn.* **2016**, *66*, 27–39. [[CrossRef](#)]
34. Ji, Y.; Zhang, J.; Wang, Y.; Yue, C.; Gong, W.; Liu, J.; Sun, H.; Yu, C.; Li, M. Coast-Ship Bistatic HF Surface Wave Radar: Simulation Analysis and Experimental Verification. *Remote Sens.* **2020**, *12*, 470. [[CrossRef](#)]
35. Yao, G.; Xie, J.; Huang, W. First-order ocean surface cross-section for shipborne HFSWR incorporating a horizontal oscillation motion model. *IET Radar Sonar Navig.* **2018**, *12*, 973–978. [[CrossRef](#)]
36. Yao, G.; Xie, J.; Huang, W. HF radar ocean surface cross section for the case of floating platform incorporating a six-DOF oscillation motion model. *IEEE J. Ocean. Eng.* **2020**, *46*, 156–171. [[CrossRef](#)]
37. Yao, G.; Xie, J.; Huang, W. Ocean surface cross section for bistatic HF radar incorporating a six DOF oscillation motion model. *Remote Sens.* **2019**, *11*, 2738. [[CrossRef](#)]
38. Barrick, D. Networking multiple HF radar systems with common coverage overlap. In Proceedings of the OCEANS'93, Victoria, BC, Canada, 18–21 October 1993.
39. Roarty, H.; Glenn, S.; Kohut, J.; Gong, D.; Handel, E.; Rivera, E.; Garner, T.; Atkinson, L.; Brown, W.; Jakubiak, C.; et al. Operation and application of a regional high-frequency radar network in the Mid-Atlantic Bight. *Mar. Technol. Soc. J.* **2010**, *44*, 133–145. [[CrossRef](#)]
40. Fujii, S.; Heron, M.L.; Kim, K.; Lai, J.W.; Lee, S.H.; Wu, X.; Wu, X.; Wyatt, L.R.; Yang, W.C. An overview of developments and applications of oceanographic radar networks in Asia and Oceania countries. *Ocean Sci. J.* **2013**, *48*, 69–97. [[CrossRef](#)]
41. Whelan, C.; Hubbard, M. Benefits of multi-static on HF Radar networks. In Proceedings of the OCEANS 2015—MTS/IEEE Washington, Washington, DC, USA, 19–22 October 2015; pp. 1–5.

42. Harlan, J.; Terrill, E.; Hazard, L.; Otero, M.; Roarty, H. The integrated ocean observing system HF radar network. In Proceedings of the OCEANS 2015—MTS/IEEE Washington, Washington, DC, USA, 19–22 October 2015; IEEE: Piscataway, NJ, USA, 2015; pp. 1–4.
43. Roarty, H.; Cook, T.; Hazard, L.; Harlan, J.; Cosoli, S.; Wyatt, L.; Alvarez Fanjul, E.; Terrill, E.; Otero, M.; Largier, J.; et al. The global high frequency radar network. *Front. Mar. Sci.* **2019**, *6*, 164. [[CrossRef](#)]
44. Stewart, R.H.; Joy, J.W. HF radio measurements of surface currents. *Deep. Sea Res. Oceanogr. Abstr.* **1974**, *21*, 1039–1049. [[CrossRef](#)]
45. Ha, E.C. Remote Sensing of Ocean Surface Current and Current Shear by HF Backscatter Radar. Ph.D. Dissertation, Stanford University, Stanford, CA, USA, 1979.
46. Teague, C.; Vesecky, J.; Hallock, Z. A comparison of multifrequency HF radar and ADCP measurements of near-surface currents during COPE-3. *IEEE J. Ocean. Eng.* **2001**, *26*, 399–405. [[CrossRef](#)]
47. Teague, C.; Vesecky, J.; Hallock, Z. Effective depth of HF current measurements: observations from COPE-3. In Proceedings of the IGARSS IEEE 2001 International Geoscience and Remote Sensing Symposium (Cat. No.01CH37217), Sydney, NSW, Australia, 9–13 July 2001; Volume 3, pp. 1134–1136.
48. Wang, J.; Dizaji, R.; Ponsford, A. An analysis of phase array radar system on a moving platform. In Proceedings of the 2005 IEEE International Radar, Conference Record, Arlington, VA, USA, 9–12 May 2005; pp. 316–320.
49. Chang, G.; Li, M.; Xie, J.; Zhang, L.; Yu, C.; Ji, Y. Ocean Surface Current Measurement Using Shipborne HF Radar: Model and Analysis. *IEEE J. Ocean. Eng.* **2016**, *41*, 970–981. [[CrossRef](#)]
50. Strang, G. *Linear Algebra and Its Application*; Academic Press: New York, NY, USA, 1976.
51. Barrick, D.; Lipa, B. Using antenna patterns to improve the quality of SeaSonde HF radar surface current maps. In Proceedings of the IEEE Sixth Working Conference on Current Measurement (Cat. No.99CH36331), San Diego, CA, USA, 13 March 1999; pp. 5–8.
52. Emery, B.M.; Washburn, L.; Harlan, J.A. Evaluating Radial Current Measurements from CODAR High-Frequency Radars with Moored Current Meters. *J. Atmos. Ocean. Technol.* **2004**, *21*, 1259–1271. [[CrossRef](#)]
53. Burke, G.J.; Poggio, A.J. Numerical Electromagnetics Code (NEC)-Method of Moments. A User-Oriented Computer Code for Analysis of the Electromagnetic Response of Antennas and Other Metal Structures. Part 1: Program Description-Theory. Part 2: Program Description-Code. Volume 1. Revised. *STIN* **1981**, *81*, 22263.
54. Turetken, B.; Ustuner, F.; Demirel, E.; Dagdeviren, A. EMI/EMC analysis of shipboard HF antenna by moment method. In Proceedings of the 2006 International Conference on Mathematical Methods in Electromagnetic Theory, Kharkiv, Ukraine, 26–29 June 2006; IEEE: Piscataway, NJ, USA, 2006; pp. 350–352.
55. Shi, J.; Jin, Z.; Li, J.; Zuo, Y. Antenna Pattern Prediction for Ship-borne VHF Communication based on MOM/PO. In Proceedings of the 2018 IEEE Asia-Pacific Conference on Antennas and Propagation (APCAP), Auckland, New Zealand, 5–8 August 2018.
56. Shi, X.; Xu, X.; Shi, Z.; Tang, Z. Measurements of the Cross-Loop Antenna Patterns in High-Frequency Surface Wave Radars. *IEEE Geosci. Remote. Sens. Lett.* **2015**, *12*, 1272–1276.
57. Xie, J.; Yuan, Y.; Liu, Y. Experimental analysis of sea clutter in shipborne HFSWR. *IEE Proc. Radar Sonar Navig.* **2001**, *148*, 67–71. [[CrossRef](#)]
58. Xie, J.; Sun, M.; Ji, Z. First-order ocean surface cross-section for shipborne HFSWR. *Electron. Lett.* **2013**, *49*, 1025–1026. [[CrossRef](#)]